Wafer Bonded Subwavelength Metallo-Dielectric Laser

O. Bondarenko,[1] A. Simic,[2] Q. Gu,[1] J. H. Lee,[1] B. Slutsky,[1] M. P. Nezhad,[1] *Member, IEEE*, and Y. Fainman,[1] *Member, IEEE*

(Invited Paper)

[1]Department of Electrical and Computer Engineering, University of California, San Diego, La Jolla, CA 92063 USA
[2]Department of Physics, University of California, San Diego, La Jolla, CA 92063 USA

DOI: 10.1109/JPHOT.2011.2146763

Manuscript received February 27, 2011; revised April 11, 2011; accepted April 19, 2011. Date of current version June 28, 2011. This work was supported by the Defense Advanced Research Projects Agency, the National Science Foundation (NSF), the NSF Center for Integrated Access Networks of Engineering Research Centers, Cymer Corporation, and the U.S. Army Research Office. Corresponding author: O. Bondarenko (e-mail: bondaren@ece.ucsd.edu).

Abstract: Light sources that are compatible with the silicon photonics platform are the key elements needed for photonic integrated circuits on silicon. Here, we report optically pumped wafer bonded metallodielectric lasers, subwavelength in all three dimensions (250-nm gain core radius) operating at 77 K, as well as near-subwavelength (450-nm gain core radius) operating at room temperature.

Index Terms: Semiconductor lasers, engineered photonic nanostructures, nanostructures, subwavelength structures, nanocavities, fabrication and characterization.

1. Introduction

Realization of silicon compatible active optical components is critical for creating integrated silicon photonic circuits and is a major step toward integration with complementary metal–oxide semiconductor-compatible platforms. Silicon has good thermoconductive properties, high quality oxide, and low cost and is available in high-quality wafers, making it invaluable for integrated electrical circuits and waveguides. Unfortunately, the indirect bandgap of silicon poses a fundamental barrier to enabling light amplification and stimulated emission in this material. Successful advances toward overcoming this limitation include demonstration of silicon Raman lasers [1] and light emission in silicon-based nanoengineered materials [2]. However, Raman laser operation is based on optical scattering, which makes it essentially limited to operation under external optical pumping. Silicon nanostructures, in turn, suffer from low gain and, therefore, low efficiency.

An alternative solution is to build hybrid optical devices through integration of III–V gain with silicon [3] using wafer bonding. III–V semiconductor compounds offer the benefits of a direct energy bandgap with wide achievable range and high carrier mobility. This makes the III–V material system optimal for active optical elements and logical devices such as lasers, switches, and modulators.

In addition to integration with silicon, another major goal of current photonics research is to reduce device footprints. Miniaturization is of great importance for the realization of compact photonic circuits for optical interconnects on-chip optical communication and sensing. Many applications often require high-density packaging of laser structures, and therefore, 3-D minimization of the lasers is ultimately desired. To date, several different subwavelength lasing structures were

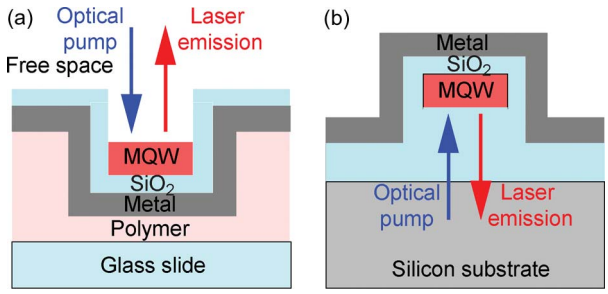

Fig. 1. (a) Scheme of the original subwavelength metallo-dielectric laser setup as from [9]. (b) Scheme of a wafer bonded metallo-dielectric laser to be reported in this paper.

reported by a few research groups [4]–[9], but integration of subwavelength lasers with passive silicon photonics still remains a challenge.

Earlier, we demonstrated room-temperature operation in subwavelength metallo-dielectric lasers [9], [10], where the dielectric shield between metal cavity and InGaAsP gain core allows us to achieve lasing at room temperature through metal loss reduction [10]. However, building a practical ultracompact on-chip device prompts us to address a few issues that include integration of the optical gain material with a silicon-on-insulator (SOI) wafer, assembly of an electrically injected laser cavity, and laser-to-waveguide mode coupling. In the original design, the nanolaser is optically pumped and mounted on a glass slide with the output light propagating in free space [see Fig. 1(a)]. The wafer bonding approach offers a path to realization of an electrically pumped subwavelength laser with vertical mode coupling to a silicon photonic waveguide by means of a slanted mirror, for example [11].

In order to exclusively investigate wafer bonding problems, we choose to keep the original cavity mode of the optically pumped nanolaser [9] intact. Thus, the III–V-to-silicon wafer bonding has to be mediated by low refractive index material, such as SiO_2, to achieve vertical mode confinement [see Fig. 1(b)]. The mediator layer has to be thick enough to reproduce the 500-nm air plug in the original design. Next, we need to select a reliable and versatile wafer bonding method, which could be used for both III–V-to-Si and III–V-to-SiO_2/Si integration.

The wide variety of available wafer bonding techniques includes fusion bonding, anodic bonding, solder bonding, eutectic bonding, thermocompression bonding, direct metal-to-metal bonding, ultrasonic bonding, low-temperature melting glass bonding, and adhesive bonding [12]. Our choice was determined by the cavity design, which required a direct low-temperature (below 400 °C) bond of an InGaAsP multiple quantum well (MQW) active layer to a silicon base. Conventional high-temperature direct wafer bonding (fusion bonding) is known to have an adverse effect on the III–V layer quality due to a thermal expansion constant mismatch of the bonded materials. Some of the available low-temperature wafer bonding methods may be useful but would require additional studies of the bonding mediator's optical and material properties (adhesive wafer bonding), its possible chemical interaction with the gain layer (anodic wafer bonding), and incorporation of these new layers into the original nanolaser model.

Recently, Liang *et al.* reported a plasma assisted wafer bonding method [13], [14], which they successfully used for realization SOI-compatible optoelectronic devices [3]. Hence, in this work, we demonstrate a silicon-compatible metallodielectric nanolaser and investigate the feasibility of this fabrication approach for integration of the device with silicon photonics platform.

2. Design and Simulations

Microdisk resonators with conventional whispering gallery mode (WGM) designs can be reduced to subwavelength scale [15], but the corresponding mode for the small structure is loosely bound, such that its evanescent tail is spread far beyond the physical resonator boundaries. This creates two problems. First, it increases the threshold requirements since the mode/gain overlap is

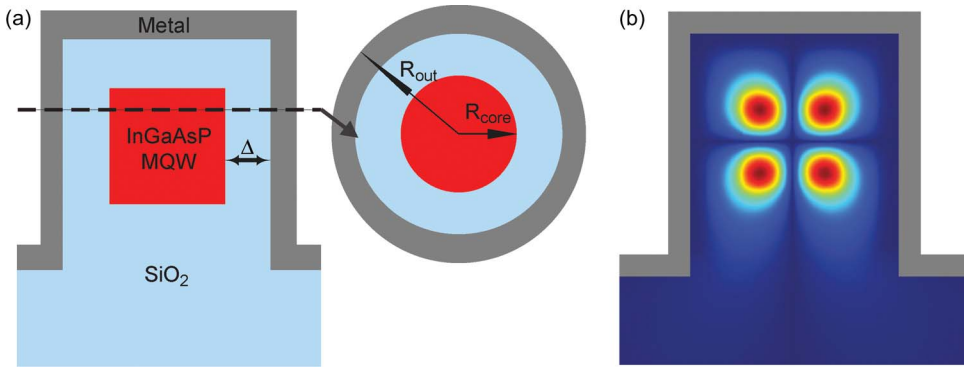

Fig. 2. (a) Schematic drawing of the wafer bonded metallo-dielectric resonator design. (b) FEM simulation of TE_{021} mode in metallo-dielectric resonator with $R_{out} = 460$ nm optimized for 1550-nm wavelength.

TABLE 1

Multiple quantum well InGaAsP/InP epitaxial structure

Name	Material	Thickness (A)	Number of layers
Capping layer	InP	100	1
Active region	1.3 Q $In_xGa_{1-x}As_yP_{1-y}$	200	16
	1.6 Q $In_xGa_{1-x}As_yP_{1-y}$	100	16
	1.3 Q $In_xGa_{1-x}As_yP_{1-y}$	200	1
Substrate	InP	~325 micron	

reduced. Second, coupling between the modes of neighboring resonators makes the WGM resonators unsuitable for densely packed laser arrays. These issues can be solved by enclosing the semiconductor resonator in a metal cavity [4]. While the metal cavity introduces strong mode confinement and thereby increases the mode/gain overlap, it also introduces high Ohmic losses. The last circumstance poses a difficulty on the way to room temperature lasing in subwavelength metallic resonators. Our approach to overcoming the metal losses is to incorporate a dielectric shield layer between the metal and semiconductor [10]. The shield thickness can be optimized for a fixed outer diameter of the laser. For an optimum shield thickness the losses reduce such that threshold gain is small enough for room temperature operation. In this case, we are still benefiting from the metal confinement, but the dielectric shield separates the largest portion of the mode, which is concentrated in the high index gain core ($\sim$3.5 for bulk InGaAsP), from direct interaction with the metal. Excessive shield thickness is detrimental, because the dielectric layer takes space that could otherwise be filled with the gain medium.

Here, we attempt to adapt this approach for an InGaAsP MQW gain layer, which is wafer bonded to SiO_2/Si (silicon wafer with thermally grown silicon dioxide layer), using our original design for the InGaAsP/InP material system. Fig. 2(a) shows a schematic of a sample metallo-dielectric nanolaser, which is optimized for minimum lasing threshold at a nominal wavelength of 1550 nm and outer radius of the resonator $R_{out} = 460$ nm. For a structure of these dimensions, the optimal shield thickness (Δ) and gain core radius (R_{core}) are 200 nm and 250 nm, respectively [10]. The gain core of the laser consists of InGaAsP with MQW (the actual composition of the gain layer is summarized in Table 1). A layer of metal (silver) confines the electromagnetic fields within the cavity. The gain is separated from the metal by a shield layer of low-index dielectric (SiO_2). The dielectric regions with low effective index above and below the gain cylinder ("plugs") provide vertical confinement of the resonator mode, as the lasing mode is in cutoff there. The lower plug is

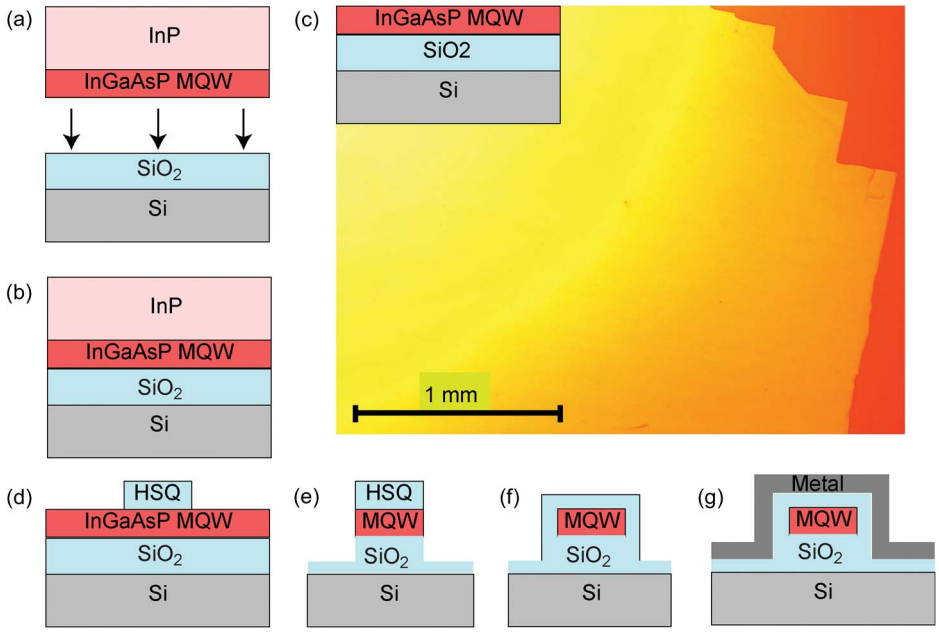

Fig. 3. Fabrication steps of a wafer bonded metallo-dielectric laser. (a) Wafer bonding of InGaAsP to SiO_2/SI, (b) resultant InP/InGaAsP/SiO_2/Si structure, (c) wet etching of InP substrate and the optical microscope image of 500-nm InGaAsP MQW layer bonded to SiO_2/Si chip, (d) e-beam lithography patterning, (e) laser pillar after two step RIE of InGaAsP and SiO_2, (f) PECVD of SiO_2 shield, and (g) metal sputtering (silver).

comprised of thermal SiO_2, in contrast with the original air plug from our previous work. This setup introduces no significant changes in the design, since the refractive index of SiO_2 is only slightly higher (1.46 versus unity for air). Finite element method (FEM) simulation of the laser resonator is shown in Fig. 2(b). The dielectric layer has been optimized for the TE_{012} mode, which has higher wavelength cutoff compared with the other lower order modes, but has the lowest achievable threshold gain of 36 cm^{-1} for the designed structure [10].

3. Fabrication

The wafer bonded subwavelength metallo-dielectric structures are fabricated from an InGaAsP MQW gain layer, bonded to a silicon wafer with a SiO_2 layer on top. The complete fabrication scheme is outlined in Fig. 3. The silicon wafers have a 6 μm thermally grown oxide layer on the surface. The MQW InGaAsP/InP wafer was ordered from OEpic Semiconductor, Inc. This gain layer is comprised of 16, 10-nm-thick, wells (1.6Q $In_xGa_{1-x}As_yP_{1-y}$, $x = 0.56$, $y = 0.938$) embedded in 17, 20-nm-thick, barriers (1.3Q $In_xGa_{1-x}As_yP_{1-y}$, $x = 0.734$, $y = 0.571$), epitaxially grown on an InP substrate that is $\approx$500 nm thickness in total (Table 1). InGaAsP MQW active layer bonding to the SiO_2/Si was accomplished through low-temperature plasma assisted wafer bonding [see Fig. 3(a)–(c)]. The process is adapted from the III–V-to-Si bonding procedure recently developed by Liang *et al.* [13], [14] and is described below.

The wafer bonding is performed for an InGaAsP/InP chip of $\sim$1 cm^2 area and a SiO_2/Si chip of $\sim$2 cm^2 area. The low-temperature bonding starts with ultrasonication of the cleaved wafers in solvents to remove all particles that would inhibit interaction between the surfaces. InGaAsP/InP is dipped in HCl for 10 s prior to the wafer bonding to remove the InP capping layer. Ultrasonication in acetone and isopropanol (IPA), followed by thorough DI water rinse, are necessary to eliminate particles from the bonding surfaces. This is a crucial step, since a single 1-μm particle results in an unbonded area of 1 cm^2 [16]. Next, the surfaces are to be stripped of native oxides, organic, and ionic contaminations. The chemical treatment is performed using standard RCA

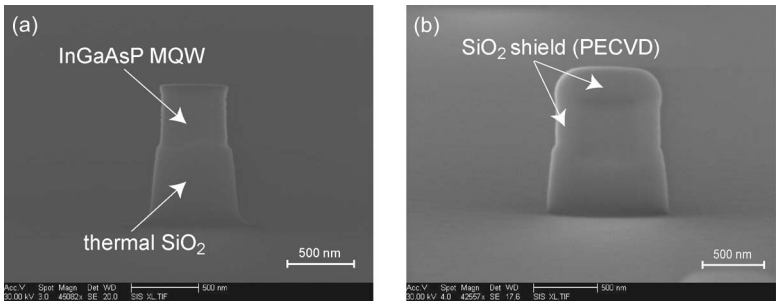

Fig. 4. SEM pictures of (a) a laser pillar after two step RIE and (b) the same pillar after PECVD of 200-nm-thick SiO_2 layer.

clean $(NH_4OH : H_2O_2 : H_2O = 1 : 2 : 10)$ for 10 min at 65–75 °C on the InGaAsP/InP chip and modified RCA clean $(HCl : H_2O_2 : H_2O = 0.2 : 1 : 5)$ for 10 min at 80 °C on the SiO_2/Si chip. Then, the InGaAsP/InP chip is immersed into NH_4OH to remove any native oxides and small contaminants left from the previous step, while SiO_2/Si is treated in $H_2SO_4 : H_2O$ (3 : 1) for 10 min to strip any traces of organic contaminants. The chemical clean is followed by ultrasonication in acetone, IPA, thorough DI water rinse, and drying in N_2 flow. After cleaning, both chips undergo O_2 plasma surface activation in a Trion reactive ion etch (RIE) chamber with 20 mTorr pressure, 30 sccm O_2 flux, and 50 W RF power for 45 s. The oxygen plasma treatment is immediately followed by a brief rinse in DI water to passivate the active surfaces with hydroxyl ($-$OH) groups. The water flow also takes away any new particles that may have accumulated during the plasma activation. Next, nitrogen flow-dried chips are manually mated. The Van der Waals force between the $-$OH groups promotes spontaneous mating of activated surfaces. The pair is annealed for 17 hours at 300 °C in an oven to form strong covalent bonding and encourage out-diffusion of the H_2O and H_2 byproducts through the thick SiO_2 layer from the InGaAsP/SiO_2 interface. Finally, the InP carrier substrate is selectively etched by HCl from the bonded sample to obtain the composite InGaAs/SiO_2/Si structure [see Fig. 3(c)].

The next step is to perform a double step RIE, which has to be carried out on the gain layer and SiO_2 using appropriate etching chemistry for each of the two materials. E-beam lithographic processing was performed on hydrogen silsesquioxane (HSQ) negative resist to create a mask [see Fig. 3(d)]. This is followed by the two-step RIE to form the cylindrical gain core and bottom SiO_2 plug. First, the 500-nm-thick InGaAsP MQW layer is dry etched in $CH_4/H_2/Ar$ (4 : 40 : 20 sccm) chemistry. Then, the SiO_2 layer undergoes CHF_3/Ar (25/25 sccm) RIE to obtain a 500-nm-tall SiO_2 post (Fig. 3(e) depicts a schematic drawing of the structure after both these steps are performed). The HSQ mask is removed during the last fabrication step along with SiO_2, since its chemical composition is quite similar to that of SiO_2. Next, the sample is treated in microwave oxygen plasma (Tepla 100) to eliminate polymer buildup. An SEM image of a sample laser after the cleaning is presented in Fig. 4(a). Next, PECVD of 200-nm-thick SiO_2 is carried out to form the low index shield around the InGaAsP core [see Fig. 3(f)]. An SEM image of the resulting structure is shown in Fig. 4(b). In the final step, we sputtered silver using a Denton Discovery 18 sputterer on the sample to complete a laser cavity [see Fig. 3(g)].

4. Measurements

We use a standard microphotoluminescence setup for optical characterization of the wafer bonded nanolasers. For optical pumping we employ a 1064-nm pulsed fiber laser which has a repetition rate of 300 kHz and 12 ns pulse width. The pump beam was focused down to an approximately 8 μm diameter spot size (FWHM) at the sample aperture plane, using a 20$\times$ microscope objective. The beam intensity profile was observed using an infrared (IR) InGaAs camera (Indigo Alpha NIR). The profile, together with the measured pump power, allowed us to estimate the peak pump intensity. The light emitted by a nanolaser is collected with the same objective and passed to the detection

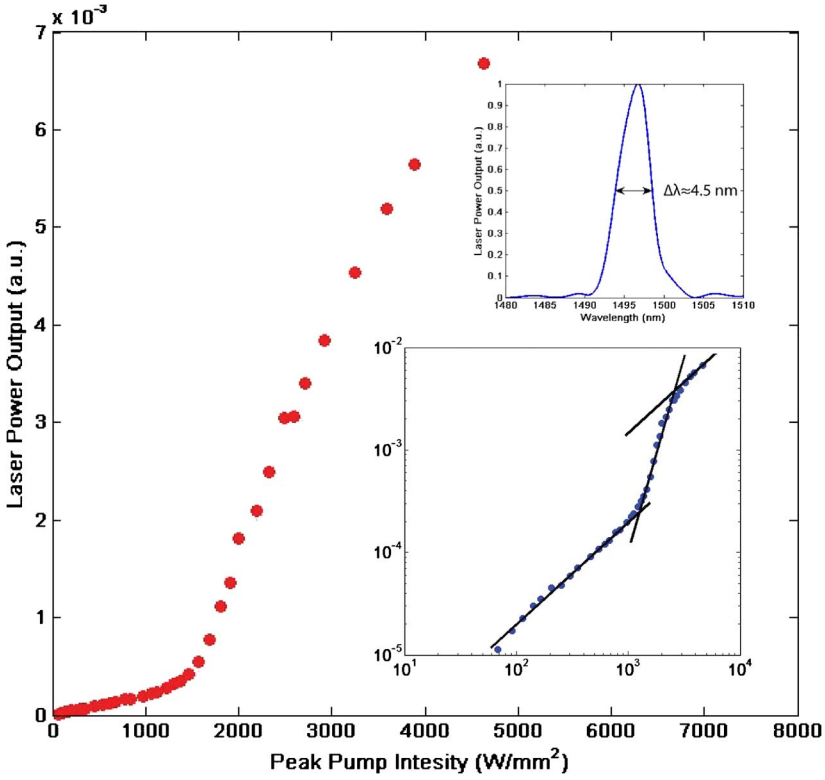

Fig. 5. Room temperature light–light curve for a nanolaser with gain core radius of $R_{core} \approx 450$ nm. The same data set is shown in the bottom inset as a log–log plot. The upper inset is the lasing spectrum taken with spectrometer; measured linewidth is 4.5 nm.

system. Using a double 4-f imaging system in conjunction with a pump filter (Semrock RazorEdge long wavelength pass), the samples are imaged onto either the IR camera, an electrically cooled InGaAs detector, or a monochromator (Spectral Products DK480) with a resolution of 0.35 nm, equipped with a cooled InGaAs detector in a lock-in detection configuration. Total power measurements for the light–light curves are performed using a single InGaAs detector. The monochromator is utilized for high-resolution measurements in lasing mode to obtain the stimulated emission peak linewidth. Optical measurements at 77 K are performed using a Janis ST-500 cryogenic chamber.

The resonant modes of the structures were found to deviate from the design 1550-nm wavelength by over 100 nm due to a variety of fabrication factors including slight ellipticity, deviation from nominal size, and sidewall curvature. For characterization, we selected devices with resonant modes close to 1550 nm, where the InGaAsP MQW material has maximum gain, since these devices may be expected to perform best. Permanent performance degradation has been observed in most devices after prolonged exposure to high pump powers. We speculate that high pump powers cause damage to the gain core. Since the light–light curves provide more conclusive evidence of lasing than linewidth measurements, we have carried out light–light measurement first. This made subsequent linewidth measurements unreliable in some cases, particularly for smaller devices.

We observed room temperature lasing from a sample with approximate gain core radius $R_{core} \approx 450$ nm and peak wavelength of 1496 nm. A kink in the linear scale light–light curve (see Fig. 5) indicates the onset of lasing at the external threshold pump intensity of 1100 W/mm^2. The same data set is shown in a log–log plot in the inset graph. For an ideal laser, the S-shaped curve represents the transition from photoluminescence (PL) mode (the lower linear section with slope 1) through amplified spontaneous emission (ASE) mode (linear section with a slope steeper than 1) into stimulated emission mode (also slope 1). The unity slope indicates a linear dependence of

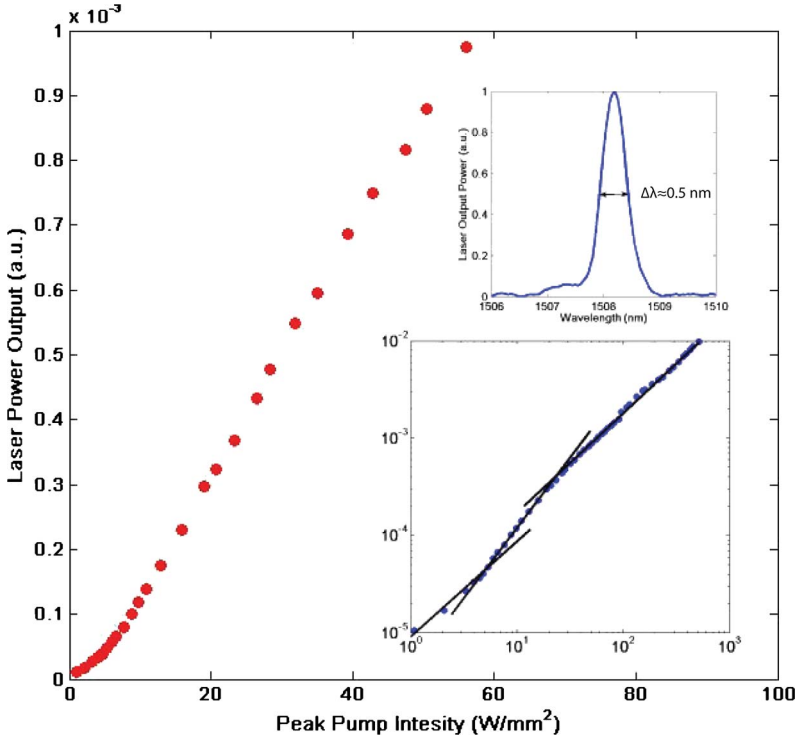

Fig. 6. Light–light curve for a nanolaser with gain core radius of $R_{core} \approx 450$ nm at 77 K. The same data set is shown in the bottom inset graph as a log–log plot. The upper inset is the lasing spectrum taken with monochrometer; measured linewidth is 0.5 nm.

output power on input pump power. The stimulated emission spectrum (see the upper inset in Fig. 5) has been measured after the light–light curve and is probably affected by material degradation discussed earlier. Other similar sized devices exhibited RT linewidths between ~1.5 and 5 nm.

Room temperature lasing from smaller samples ($R_{core} \approx 250$ nm) exhibited severe drop of the stimulated emission peak intensity over time, especially after the samples had been subjected to high pump powers. That prevented reliable light–light curve measurements of small (subwavelength) samples. To achieve lasing at lower pumping levels, we also performed optical measurements at 77 K, with samples placed in a cryogenic chamber. The light–light curves for both $R_{core} \approx 450$ nm (see Fig. 6) and 250 nm (see Fig. 7) are presented, with the corresponding log–log curves in the inset graphs.

For the nanolaser with $R_{core} \approx 450$ nm and peak wavelength of 1508 nm, the threshold at 77 K is reduced to 100 W/mm^2, which is approximately 10 times lower compared with the RT results for a sample of the same geometry. The linewidth is measured to be 0.5 nm, from the high-resolution spectrum shown in the upper inset of Fig. 6. The significant linewidth narrowing at 77 K compared with the room temperature width is an expected phenomenon, which originates from reduced cavity losses, increased output power [17] and smaller linewidth enhancement factor [18]. The smooth ASE transition region and reduced threshold pump density of the S-curve at 77 K result from increased material gain, suppressed spectral broadening, enhanced cavity Q, and much lower nonradiative recombination rates at cryogenic temperatures [17], [19].

For the 250-nm sample, the lasing wavelength at 77 K is 1527 nm, and the threshold is about 12 W/mm^2, as shown in Fig. 7. The emission spectrum of this sample, measured after the light–light curve, was severely affected by material degradation and is not shown. The slope of the PL-related linear part of the log–log curve (see the inset of Fig. 7) is around 1.2, in contrast to the samples with $R_{core} \approx 450$ nm, for which the slope is close to unity. The PL region slope larger than

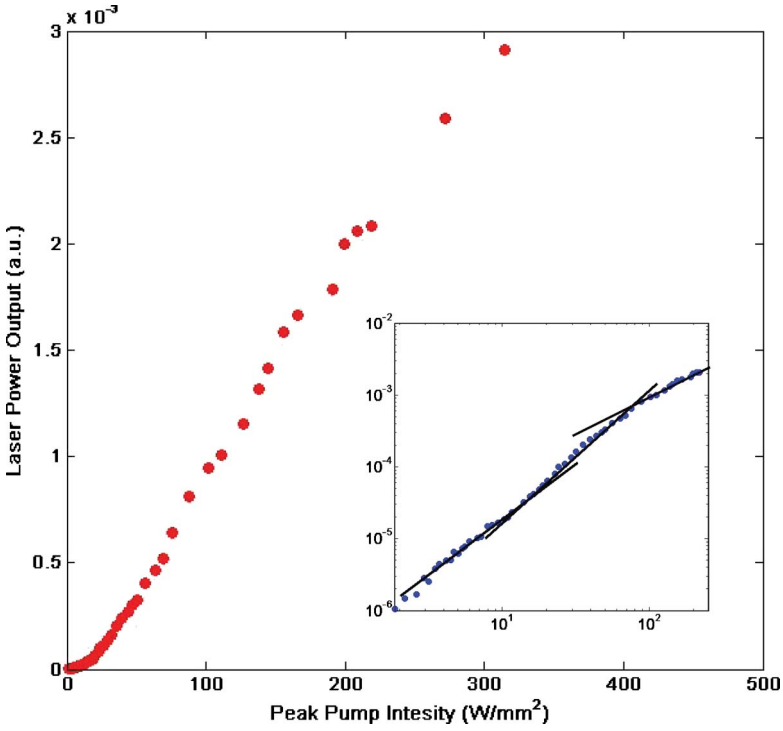

Fig. 7. Light–light curve for a laser with $R_{core} \approx 250$ nm at 77 K with the corresponding log–log plot in the inset graph.

unity indicates that a significant fraction of recombination events is caused by single-particle nonradiative processes, such as surface recombination [20]. In the smaller nanolasers, surface recombination is likely to be responsible for the high PL slope, since the ratio of the gain core surface area to its volume for the sample with $R_{core} \approx 250$ nm is much greater than the surface/volume ratio for the sample with $R_{core} \approx 450$ nm and, thereby, must introduce many more nonradiative recombination centers. Along with the problem of dramatic drop in stimulated emission intensity under optical pumping at room temperature, this is an interesting issue to be further investigated.

5. Conclusion

In this paper, we demonstrate a wafer bonded subwavelength scale laser that can be integrated onto a silicon platform. We observe room temperature lasing from near-subwavelength structures with gain core radius $R_{core} \approx 450$ nm and cryogenic temperature operation for subwavelength structures with R_{core} of 250 nm. The results for the optically pumped lasers are expected to improve through further optimization of the fabrication process.

We believe that our approach to realization of subwavelength scale coherent sources, combined with the latest III–V-to-Si wafer bonding solutions, is a promising path for the realization of highly integrated and miniaturized room temperature silicon photonic devices. In addition, our unique metal-dielectric resonator design is of interest for a number of applications, such as on-chip communication, optical interconnects, sensing, and storage.

Acknowledgment

The authors would like to acknowledge helpful discussions with representatives of OEpic Semiconductors, Inc., and members of Optoelectronic Research Group at UC Santa Barbara.

References

[1] H. Rong, R. Jones, A. Liu, O. Cohen, D. Hak, A. Fang, and M. Paniccia, "A continuous-wave Raman silicon laser," *Nature*, vol. 433, no. 7027, pp. 725–728, Feb. 17, 2005.

[2] L. Dal Negro, "Light emission from silicon nanostructures: Past, present and future perspectives," in *Proc. OSA/CLEO/IQEC*, 2009, pp. 1–2.

[3] A. W. Fang, H. Park, O. Cohen, R. Jones, M. J. Paniccia, and J. E. Bowers, "Electrically pumped hybrid AlGaInAs-silicon evanescent laser," *Opt. Express*, vol. 14, no. 20, pp. 9203–9210, Oct. 2006.

[4] M. T. Hill, Y. S. Oei, B. Smalbrugge, Y. Zhu, T. de Vries, P. J. van Veldhoven, F. W. M. van Otten, T. J. Eijkemans, J. S. P. Turkiewicz, H. de Waardt, E. J. Geluk, S. H. Kwon, Y. H. Lee, R. Nötzel, and M. K. Smit, "Lasing in metallic-coated nanocavities," *Nat. Photon.*, vol. 1, no. 10, pp. 589–594, Oct. 2007.

[5] K. Yu, A. Lakhani, and M. C. Wu, "Subwavelength metal-optic semiconductor nanopatch lasers," *Opt. Express*, vol. 18, no. 9, pp. 8790–8799, Apr. 2010.

[6] R. F. Oulton, V. J. Sorger, T. Zentgraf, R. M. Ma, C. Gladden, L. Dai, G. Bartal, and X. Zhang, "Plasmon lasers at deep subwavelength scale," *Nature*, vol. 461, no. 7264, pp. 629–632, Oct. 2009.

[7] H. G. Park, S. H. Kim, S. H. Kwon, Y. G. Ju, J. K. Yang, J. H. Baek, S. B. Kim, and Y. H. Lee, "Electrically driven single-cell photonic crystal laser," *Science*, vol. 305, no. 5689, pp. 1444–1447, Sep. 2004.

[8] R. Ma, R. F. Oulton, V. J. Sorger, G. Bartal, and X. Zhang, "Room-temperature sub-diffraction-limited plasmon laser by total internal reflection," *Nat. Mater.*, vol. 10, no. 2, pp. 110–113, Feb. 2011.

[9] M. P. Nezhad, A. Simic, O. Bondarenko, B. Slutsky, A. Mizrahi, L. Feng, V. Lomakin, and Y. Fainman, "Room-temperature subwavelength metallo-dielectric lasers," *Nat. Photon.*, vol. 4, no. 6, pp. 395–399, Jun. 2010.

[10] A. Mizrahi, V. Lomakin, B. A. Slutsky, M. P. Nezhad, L. Feng, and Y. Fainman, "Low threshold gain metal coated laser nanoresonators," *Opt. Lett.*, vol. 33, no. 11, pp. 1261–1263, Jun. 2008.

[11] D. Van Thourhout, G. Roelkens, R. Baets, W. Bogaerts, J. Brouckaert, P. Debackere, P. Dumon, S. Scheerlinck, J. Schrauwen, D. Taillaert, F. Van Laere, and J. Van Campenhout, "Coupling mechanisms for a heterogeneous silicon nanowire platform," *Semicond. Sci. Technol.*, vol. 23, no. 6, p. 064004, Jun. 2008.

[12] F. Niklaus, G. Stemme, J. Q. Lu, and R. J. Gutmann, "Adhesive wafer bonding," *J. Appl. Phys.*, vol. 99, no. 3, p. 031101, Feb. 2006.

[13] D. Liang, J. E. Bowers, D. C. Oakley, A. Napoleone, D. C. Chapman, C.-L. Chen, P. W. Juodawlkis, and O. Raday, "High-quality 150 mm InP-to-silicon epitaxial transfer for silicon photonic integrated circuits," *Electrochem. Solid-State Lett.*, vol. 12, no. 4, pp. H101–H104, 2009.

[14] D. Liang, A. W. Fang, H. Park, T. E. Reynolds, K. Warner, D. C. Oakley, and J. E. Bowers, "Low-temperature, strong SiO_2–SiO_2 covalent wafer bonding for III–V compound semiconductors-to-silicon photonic integrated circuits," *J. Electron. Mater.*, vol. 37, no. 10, pp. 1552–1559, Oct. 2008.

[15] Q. Song, H. Cao, S. T. Ho, and G. S. Solomon, "Near-IR subwavelength microdisk lasers," *Appl. Phys. Lett.*, vol. 94, no. 6, p. 061109, Feb. 2009.

[16] D. Pasquariello and K. Hjort, "Plasma-assisted InP-to-Si low temperature wafer bonding," *IEEE J. Sel. Topics Quantum Electron.*, vol. 8, no. 1, pp. 118–131, Jan./Feb. 2002.

[17] L. A. Coldren and S. W. Corzine, *Diode Lasers and Photonic Integrated Circuits*. New York: Wiley-Interscience, 1995.

[18] M. Osinski and J. Buus, "Linewidth broadening factor in semiconductor lasers—An overview," *IEEE J. Quantum Electron.*, vol. QE-23, no. 1, pp. 9–29, Jan. 1987.

[19] T. Baba and D. Sano, "Low-threshold lasing and Purcell effect in microdisk lasers at room temperature," *IEEE J. Sel. Topics Quantum Electron.*, vol. 9, no. 5, pp. 1340–1346, Sep./Oct. 2003.

[20] K. Srinivasan, M. Borselli, O. Painter, A. Stintz, and S. Krishna, "Cavity Q, mode volume, and lasing threshold in small diameter AlGaAs microdisks with embedded quantum dots," *Opt. Express*, vol. 14, no. 3, pp. 1094–1105, Feb. 2006.